Journal of Structural Geology 35 (2012) 102–116

Contents lists available at ScienceDirect

Journal of Structural Geology

journal homepage: www.elsevier.com/locate/jsg

The influence of viscosity contrast on the strain pattern and magnitude within and around dense blocks sinking through Newtonian rock salt

Steffi Burchardt [a,*], Hemin Koyi [a], Harro Schmeling [b]

[a] Department of Earth Sciences, Uppsala University, Villavägen 16, 75236 Uppsala, Sweden
[b] Institute of Earth Sciences, J. W. Goethe University, Altenhöferallee 1, 60438 Frankfurt am Main, Germany

ARTICLE INFO

Article history:
Received 17 January 2011
Received in revised form
15 July 2011
Accepted 23 July 2011
Available online 16 August 2011

Keywords:
Salt
Anhydrite
Deformation
Newtonian rheology
Viscosity contrast
Gorleben

ABSTRACT

Dense inclusions in salt cover a wide range of materials and therefore material properties, depending on their origin. We have modelled the deformation associated with gravity-driven sinking of horizontal, initially rectangular blocks of dense material through Newtonian salt. Our two-dimensional Finite Differences models analyse the influence and interaction of two parameters: (1) the size, i.e. the aspect ratio (AR), of the block and (2) the viscosity contrast between the salt and the more viscous block over four orders of magnitude. The results demonstrate that during gravity-driven sinking the blocks are folded and sheared. The strain magnitude within the block increases with increasing block AR and decreases with increasing viscosity contrast. Sinking velocities of the blocks are in the range of <2 and >6 mm a^{-1} and are a function of block and salt deformation that depend on the block mass and AR, as well as on the viscosity contrast. Salt deformation is characterised by the development of an array of characteristic structures that include folds and shear zones, as well as a zone characterised by extreme vertical stretching above the block, termed entrainment channel. Strain in the salt is locally more than two orders of magnitude higher than in the block and increases with increasing block AR and viscosity contrast. Salt deformation is distributed in closely spaced high- and low-strain zones concentrated in the block vicinity and the entrainment channel.

1. Introduction

Natural salt structures contain a large variety of inclusions of different origin, size, lithology, and hence mechanical properties. Examples of such inclusions in salt cover synsedimentary layers of e.g. limestone, shale, and anhydrite (e.g. Bornemann, 1991; Schoenherr et al., 2010), volcanic rocks erupted during salt evaporation (e.g. Gansser, 1960; Kent, 1979; Weinberg, 1993), and even intrusive rocks injected into the salt. The size of these exotic blocks ranges from centimetre-size "impurities" in the salt to kilometre-scale slabs of internally intact volcanic sequences, but their shapes are often tabular as a result of their originally horizontal sedimentary or igneous layering (Gansser, 1992; Jackson et al., 1990; Weinberg, 1993).

Weinberg (1993) suggested that dense inclusions in salt structures might start to sink when ascent rates of the salt are no longer sufficient to support their weight. Experimental results by Koyi (2001) have recently stimulated a discussion about the potential of entrained exotic blocks to reactivate the internal dynamics of externally inactive salt diapirs caused by the gravity-driven sinking of the denser blocks. This process might have crucial implications for the long-term stability of sites for the storage of hazardous waste in salt diapirs, as envisaged for example in the Gorleben salt mine, Germany (Koyi, 2001; Chemia et al., 2009).

In order to understand the impact of exotic blocks on the strain field and strain evolution within the salt structure, we ran two-dimensional numerical models of a horizontal, rectangular block of higher density sinking through less dense Newtonian salt. In an earlier paper (Burchardt et al., 2011), we studied the influence of the size of the block at a constant viscosity contrast between the block and the surrounding salt of 1000. We concluded that block aspect ratio (AR) is a crucial parameter, controlling block deformation, the spatial extent and intensity of salt deformation, as well as the sinking velocity of the block. In this study, we increased the parameter space by systematically analysing the influence and interaction of two main parameters, namely the size of the block and the viscosity contrast between the block and the matrix salt. Using the results of 40 models considering viscosity contrasts varying over four orders of magnitude and block widths ranging from 100 to 1000 m, we demonstrate how the interaction between

* Corresponding author.
E-mail address: steffi.burchardt@geo.uu.se (S. Burchardt).

0191-8141/$ – see front matter © 2011 Elsevier Ltd. All rights reserved.
doi:10.1016/j.jsg.2011.07.007

both parameters influences the strain pattern and magnitude within and around the block, as well as the sinking velocity of the block.

2. Modelling background

2.1. Model setup and scaling

The setup of all models presented here comprises a rectangular reservoir of salt, 2000 m wide and 4000 m deep (Fig. 1). These dimensions are not scaled to any particular natural salt structure, but are based on general sizes of salt domes or diapirs that are usually a few kilometres tall and wide.

Inclusions of exotic material in salt diapirs often originate from synsedimentary or volcanic successions originally deposited as layers which during salt ascent are entrained as elongate boudins or blocks (cf. Weinberg, 1993). A well-studied example of a layer of dense material entrained in a salt structure is the 70 m thick Main Anhydrite, a formation containing mainly anhydrite with some minor intercalations of limestone, that was entrained in the ascent of the Upper Permian Zechstein salt in Northern Germany and, in course of this process, deformed into elongate boudins and layer fragments, partly folded within the salt (Bornemann, 1991). These layer fragments have lengths between less than 100 m and more than 1000 m. Further examples of entrained exotic material include ca. 60 m thick and several hundred metre long fragments of synsedimentary successions of carbonate rocks ("stringers") within the salt structures of Oman (Peters et al., 2003; Reuning et al., 2009), as well as limestone, dolomite, sandstone, gneiss, rhyolite, and basaltic rocks entrained as more or less tabular blocks within the salt structures of the Zagros Mountains and Great Kavir, Iran (Gansser, 1960, 1992; Kent, 1979; Jackson et al., 1990; Weinberg, 1993).

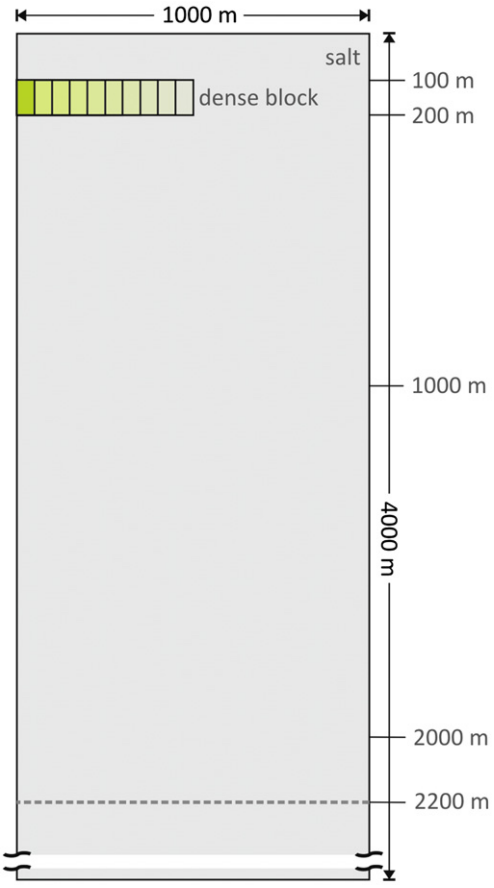

Fig. 1. Model geometry illustrating the modelled half of the setup. All model boundaries are symmetry planes and allow free slip. The grey dashed line indicates the maximum depth, to which block sinking was analysed.

In our models, a rectangular block with a thickness of 100 m is placed at a depth of 100 m below the top of the salt, its base resting at a depth of 200 m (Fig. 1). In each series of models, at a particular viscosity, the width of the block is systematically varied in increments of 100 m to result in ten different models. Hence, the thickness to width ratio (AR) of the block changes in each series of models from 1:1 (thickness 100 m, width 100 m) to 1:10 (thickness 100 m, width 1000 m).

In the models, the block sinks through the salt driven by gravity only, because the block was assigned a density of 2900 kg m^{-3} (close to the density of pure anhydrite) that exceeds the density of the surrounding salt (2200 kg m^{-3}) by 700 kg m^{-3}. For each model, only the first 2000 m of sinking of the block are analysed to avoid boundary effects from the bottom of the model. Our models assume that all materials are incompressible, homogeneous, and have a Newtonian viscosity. We therefore disregard any internal heterogeneities inherited from e.g. salt ascent or sedimentation. Furthermore, the models do not consider temperature effects. The salt is assigned a constant viscosity of 10^{17} Pa s, which is in accordance with estimations of the behaviour of fine-grained, relatively dry rock salt under natural conditions. According to Mukherjee et al. (2010, and references therein), salt can behave as a Newtonian viscous fluid with a viscosity that ranges from 10^{15} to 10^{21} Pa s, depending on a number of parameters, such as e.g. temperature, grain size, differential stress, and the presence of fluids (e.g. Urai et al., 1986, 2008). In comparison to salt, the viscosities of anhydrite and other geological materials that occur as inclusions in salt structures are not well constrained. However, their deformation behaviour can be roughly estimated from their deformed shapes after salt emplacement. Accordingly, inclusions composed of volcanic sequences with preserved primary structures and little bending at kilometre-scale in salt glaciers in the Zagros Mountains (e.g. Jackson et al., 1990) can be expected to have a high effective viscosity compared to entrained anhydrite layers folded into isoclinal folds within the salt diapirs of the North German basin (Bornemann, 1991). There are few rock-physical experiments to determine the rheological behaviour of anhydrite (e.g. Müller and Siemes, 1974; Müller et al., 1981; Zulauf et al., 2009), but they do not cover the temperatures, pressures, and strain rates relevant to natural systems. Zulauf et al. (2009) estimate the viscosity ratio of anhydrite to rock salt to be approximately 27, while Chemia et al. (2009) use viscosity contrasts that range from 100 to 10,000. In order to account for a large range of viscosity contrasts between the dense inclusion and the host material ($m = \mu_{\text{inclusion}}/\mu_{\text{matrix}}$), we systematically varied the viscosity of the block from 10^{18} Pa s to 10^{21} Pa s in four different model series, in which each series consists of ten models with varying block AR. Consequently, the effect of m can be analysed over four orders of magnitude (10–10,000).

2.2. Modelling strategy

The two-dimensional models were run using the Finite Differences code FDCON (Weinberg and Schmeling, 1992) to solve the equations of conservation of mass, momentum, and composition in plain strain. This is achieved by using a stream function formulation applying Cholesky decomposition of the symmetric matrix. From the velocity field, the movement of a compositional field is described by a mesh of marker points, the movement of which is calculated by a fourth-order Runge–Kutta algorithm combined with a predictor–corrector step. For additional details on the

governing equations, the reader is referred to Weinberg and Schmeling (1992).

Along all model boundaries, free slip was enabled to allow free flow of the salt along the boundaries and free movement of the block. In addition, since model boundaries are symmetry planes and the model geometry is axial-symmetric, only half the model geometry had to be modelled. For this, we chose a finite-differences grid with a resolution of 101 in horizontal direction and 401 in vertical direction with 1000 times 4000 markers together forming the marker field to ensure an optimal resolution. The interface between the block and the salt is adhesive, and the compositional contrast between block and matrix material is treated by defining effective parameters, i.e., the material properties density and viscosity along the boundary are derived from the arithmetic mean of each parameter. This ensures an accurate resolution of the interface. Materials are incompressible and purely viscous, and thus neglect changes in area, elastic behaviour, and inertial forces so that creeping flow is assumed.

The marker field at different time steps during sinking of the block was used to calculate and plot distribution and magnitude of strain with the free software SSPX (Cardozo and Allmendinger, 2009), based on the grid nearest-neighbour method. More specifically, the marker field of a model at the initial (undeformed) and at a later (deformed) stage is overlain by a regularly spaced grid. Dilatational and maximum shear strain γ is calculated after Ramsay and Huber (1987) at the centre of each grid cell using a defined number of nearest neighbours. For additional details on strain calculation with SSPX, the reader is referred to Cardozo and Allmendinger (2009).

3. Strain pattern and magnitudes in the sinking blocks as a function of block AR and *m*

3.1. Strain pattern in the sinking block

3.1.1. Viscosity ratio $m = 10$

In the models with a viscosity contrast between the block and the host material, $m = 10$, salt flows around the sinking blocks causes strong deformation of the blocks. In the block with an AR of 1:1, block strain is initially characterised by horizontal shortening of the upper half of the block (Fig. 2). After less than 100 m of sinking, this is accompanied by horizontal extension in the lower half of the block. Further sinking causes an additional upward drag of block material along the lower corners (and lateral margins of the block). Together, these processes cause a rapid folding of the upper block half first into a tight then isoclinal synform, while the lower half of the block is folded more slowly, but finally also reaches isoclinality (Figs. 2 and 3). Marginal shear and upward drag of block material relative to the block centre causes the initial corners of the block to finally point upwards, entraining narrow slivers of salt. Consequently, the final shape of the block with an initial AR of 1:1 is circular with upward-pointing cuspate appendices (Fig. 3).

In comparison, the block with an AR of 1:5 is immediately folded into an upright synform with progressively decreasing

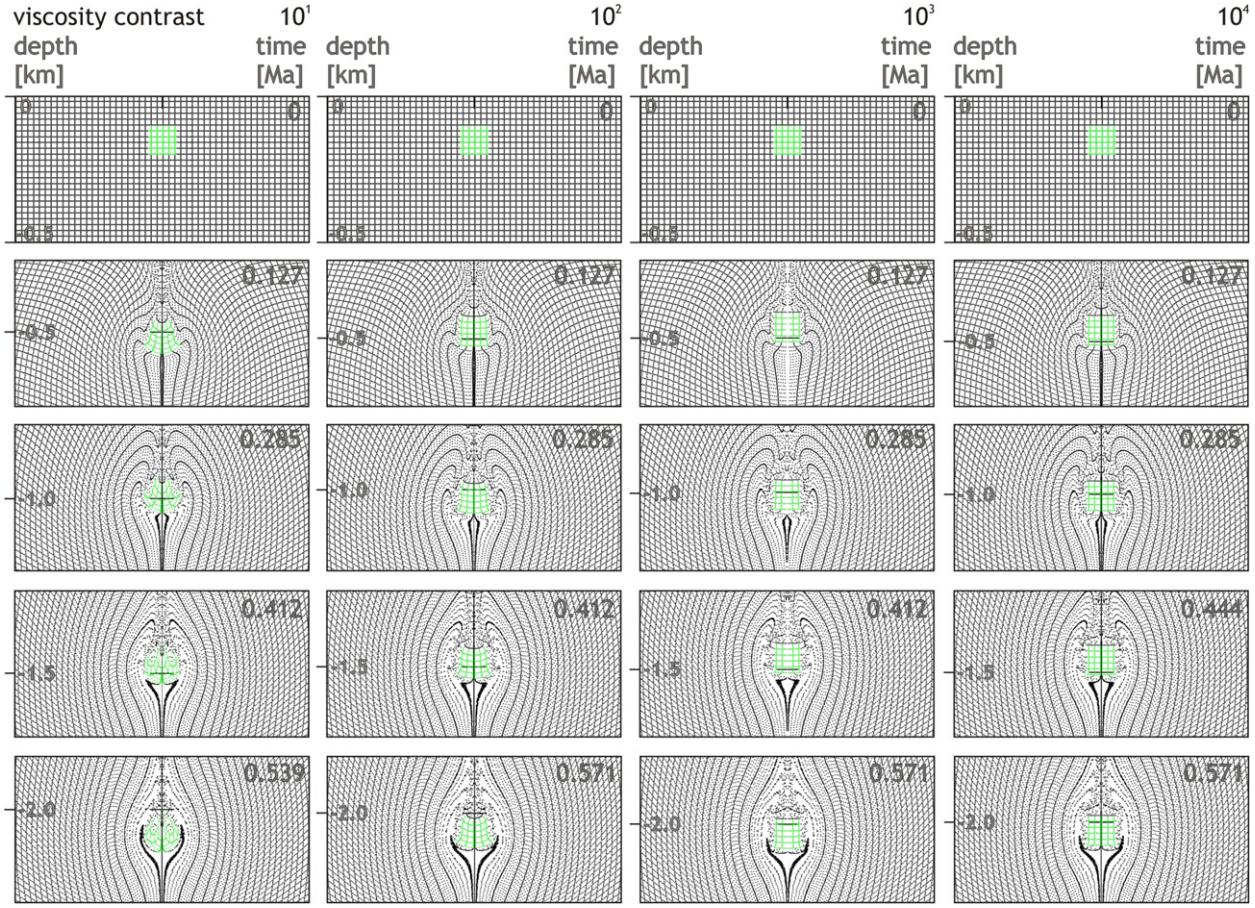

Fig. 2. Sections (1000 m wide and 500 m deep) of mesh plots displaying the strain pattern of a block (in green) with an AR of 1:1 sinking through a matrix of salt (black). The salt has a viscosity of 10^{17} Pa s, while the viscosity of the block varies in each series of models. The mesh plots display every fourth marker of the marker field of the models. (For interpretation of the references to colour in this figure legend, the reader is referred to the web version of this article.)

interlimb angle (Fig. 4). While the upper margin of the block is folded into an isoclinal fold after less than 500 m of sinking, the block is successively folded further to form a closed shape entraining a portion of salt with a width of ca. 65 m and a thickness of ca. 200 m at the final depth of sinking of the block. Furthermore, marginal shear along the outside of the folded limbs results in thinning of the upward-pointing ends of the limbs, so that the final shape of the block after 2000 m of sinking resembles a tear drop that encloses a portion of salt and has cuspate upper ends (Fig. 3).

Deformation during sinking of the block with an AR of 1:10 first results in the development of an upright fold with inward-pointing limbs and a wide hinge area (Fig. 5) as a result of maximum bending near the edges. The distance between the point of maximum bending and the upper lateral ends of the block is on the order of the block thickness, while the bending approaches zero near the centre of the block. This is in contrast to blocks with an AR of <5, for which the point of maximum bending is located in the centre of the block already at the onset of deformation. During further sinking, the width of the hinge area of the block with an AR of 1:10

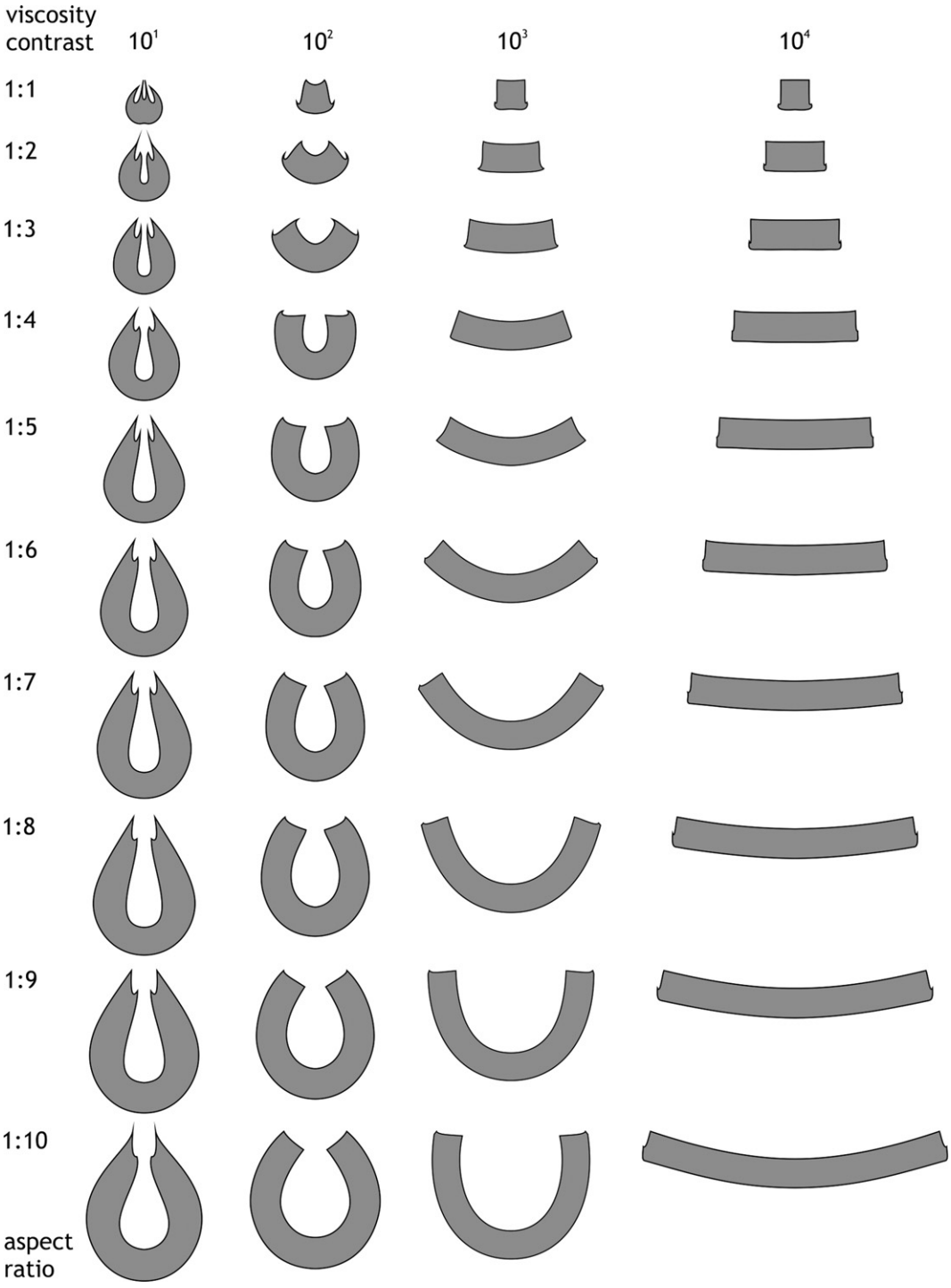

Fig. 3. Overview of the deformed shapes of the blocks of all series after 2000 m of sinking. The model series with $m = 1000$ is described in detail by Burchardt et al. (2011).

decreases and the block approaches a tear drop-like shape at 2000 m depth, enclosing a portion of salt that was originally located above the block. Marginal shear along the outside of the upward-pointing fold limbs begins to thin the lower part of the limbs. Consequently, the final shape of the block with an initial AR of 1:10 resembles a tear drop with cuspate upper ends, entraining a ca. 150 m wide and ca. 260 m deep portion of salt (Fig. 3). The final shapes of the blocks of this series of models resemble each other in their tear-drop shape with cuspate upward-pointing ends and in that they entrain portions of the initially overlying salt (Fig. 3).

3.1.2. Viscosity ratio $m = 100$

Salt flow around the blocks of the model series with $m = 100$ causes intense folding of the blocks into horse-shoe shapes. During sinking, the block with an AR of 1:1 is folded into an upright, open synform by successive horizontal shortening of the upper block half and horizontal elongation of the lower block half (Fig. 2). Shear along the lateral block sides results in the formation of cuspate appendices from the lower block corners. The final block shape is characterised by open folding with a narrower upper half (Fig. 3). The block with an AR of 1:5 is successively folded during sinking; after 500 m the block is folded into an upright, open synform (Fig. 4). During successive sinking, the fold closes to approach a horse-shoe shape with inward-pointing limbs, enclosing a portion of the initially overlying salt that is ca. 90 m wide and 170 m thick (Fig. 4). In comparison, the block with an AR of 1:10 is folded rapidly into an isoclinal synform. Folding progresses from the lateral ends of the block towards its middle, so that the hinge width of the synform decreases successively during sinking (Fig. 6). The block finally approaches a circular, then slightly oval, horse-shoe shape enclosing a portion of salt that is ca. 270 m wide and ca. 280 m thick (Fig. 3). A comparison of the final shapes of all blocks of this series shows similar horse-shoe shapes with inward-pointing fold limbs, enclosing an oval portion of salt that becomes wider with increasing block AR (Fig. 3).

3.1.3. Viscosity ratio $m = 1000$

Deformation of the blocks of the model series with $m = 1000$ (also modelled in Burchardt et al., 2011) is characterised by open to isoclinal folding. In case of the block with an AR of 1:1, salt flow causes slight horizontal elongation of the lower part of the block (ca. 20% of the block thickness is affected) and even slighter horizontal shortening in the upper marginal area of the block (Fig. 2). Marginal shear causes the lower corners of the block to become dragged upwards relative to the centre of the block. Consequently, the block is openly folded after 2000 m of sinking (Fig. 3). In comparison, the block with an AR of 1:5 is continuously folded into an upright, open synform with an interlimb angle of ca. 90° (Figs. 3 and 4), while the block with an AR of 1:10 is folded into a horse-shoe shape with the fold limbs pointing inwards, enclosing an angle of ca. 10° (Figs. 3 and 5). By this, a ca. 260 m wide and ca. 280 m thick portion of the initially overlying salt is enclosed in

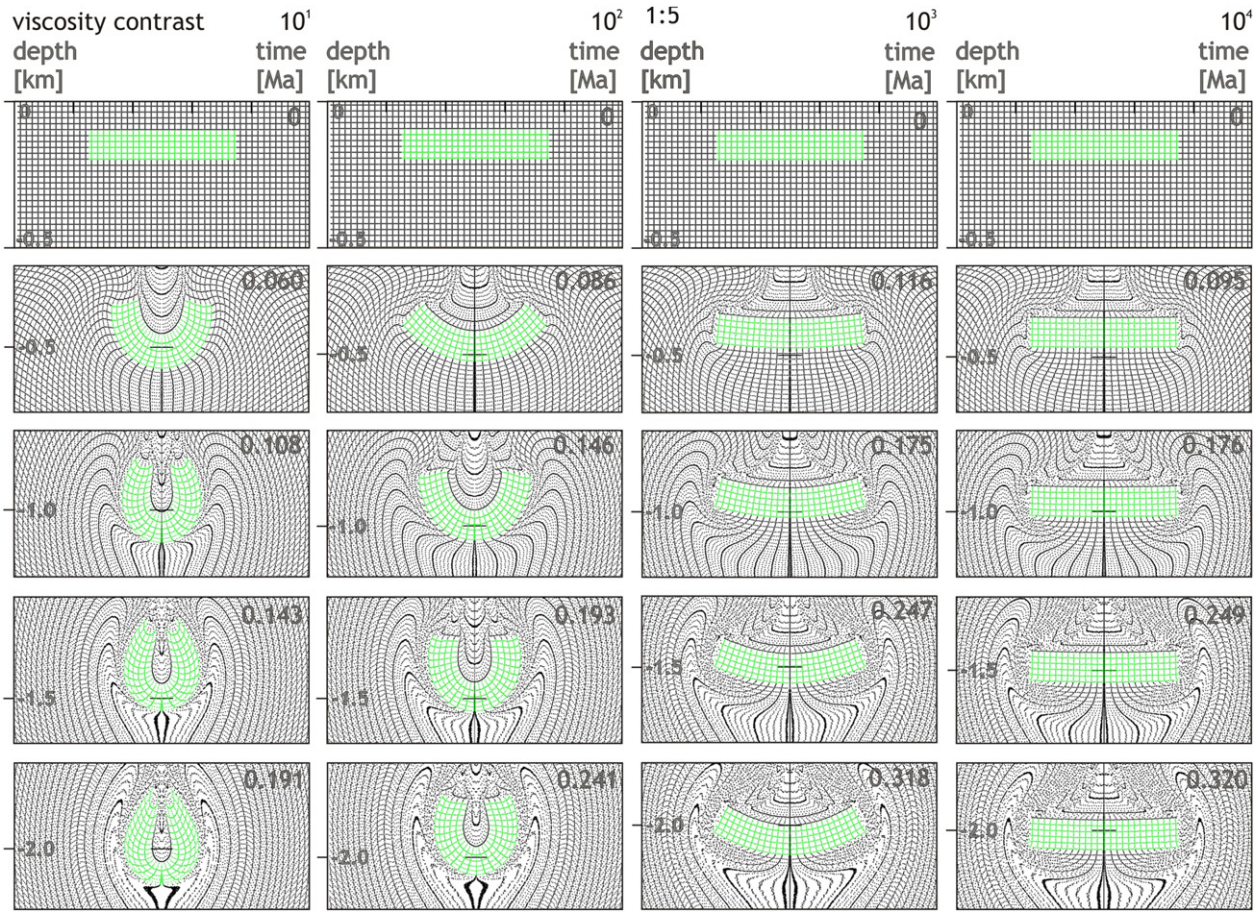

Fig. 4. Sections (1000 m wide and 500 m deep) of mesh plots displaying the strain pattern of a block (in green) with an AR of 1:5 sinking through a matrix of salt (black). The salt has a viscosity of 10^{17} Pa s, while the viscosity of the block varies in each series of models. The mesh plots display every fourth marker of the marker field of the models. (For interpretation of the references to colour in this figure legend, the reader is referred to the web version of this article.)

the fold. Hence, a comparison of the deformed shapes of the blocks of this model series shows that folding becomes more and more effective as a function of increasing block AR (Fig. 3).

3.1.4. Viscosity ratio $m = 10{,}000$

The deformation of the blocks in the model series with $m = 10{,}000$ is characterised by slight folding of the blocks during sinking. The block with an AR of 1:1 almost keeps its initial square shape (Fig. 2). Only slight horizontal elongation occurs along the lower block margin (less than 20% of the block's thickness is affected). In addition, salt flow around the block causes an upward drag of the block's lower corners relative to the block centre. Consequently, the final shape of the block resembles the initial shape with slightly dragged-up lower corners (Fig. 3). Increasing the block AR, results in a very slight increase of block deformation during sinking. The block with an AR of 1:5 shows almost no signs of deformation. Only the lower block corners become "eroded", i.e. sheared off, after a very low amount of horizontal elongation of the lower block margin as a result of viscous drag (Fig. 4). Hence, the deformed shape of the block with an initial AR of 1:5 after 2000 m of sinking shows a very weak folding and worn-off lower corners (Fig. 3). However, as the viscous deformation of sharp, high-viscosity corners due to viscous drag generally poses numerical resolution problems, we cannot quantitatively resolve the exact width and length of the cusps. The block with an AR of 1:10 first suffers erosion of the lower block corners before it is successively folded into an upright, open synform with an interlimb angle of $\sim 144^{\circ}$ (Figs. 3 and 5).

3.2. Strain magnitude and strain ellipses of the sinking block

Shear strain magnitudes and ellipses of the sinking blocks monitored during sinking show a constant increase in block strain during sinking (Fig. 6). In the models with $m = 10$, strain during sinking is characterised by a strong increase in the block centre that is subsequently accompanied by shearing parallel to the upward-bending block margins. In contrast, the interior of the block sides remains almost unstrained even at the final depth of 2200 m. Similar strain distribution during sinking but with decreasing magnitudes of strain is observed in the models with higher m (Fig. 6), i.e. at $m \geq 100$, the block does not show much internal strain. Only the central area of the block is characterised by weak horizontal shortening at the final depth of sinking.

A comparison of the block strain for blocks with different block ARs after a sinking distance of 500 m shows that block strain generally increases with increasing block AR and confirms a decrease with increasing m (Figs. 7 and 8).

3.3. Sinking velocity of the block

The deformation of the blocks during sinking is also reflected in their sinking velocity (Fig. 9) that was determined in the block centre, 30 m above the lower block margin. The first stage of sinking is characterised by an acceleration phase lasting approximately 0.15 Ma. This transient acceleration is caused by the progressively decreasing influence of the top boundary of the model (Figs. 9 and 10). After acceleration, the block with an AR of

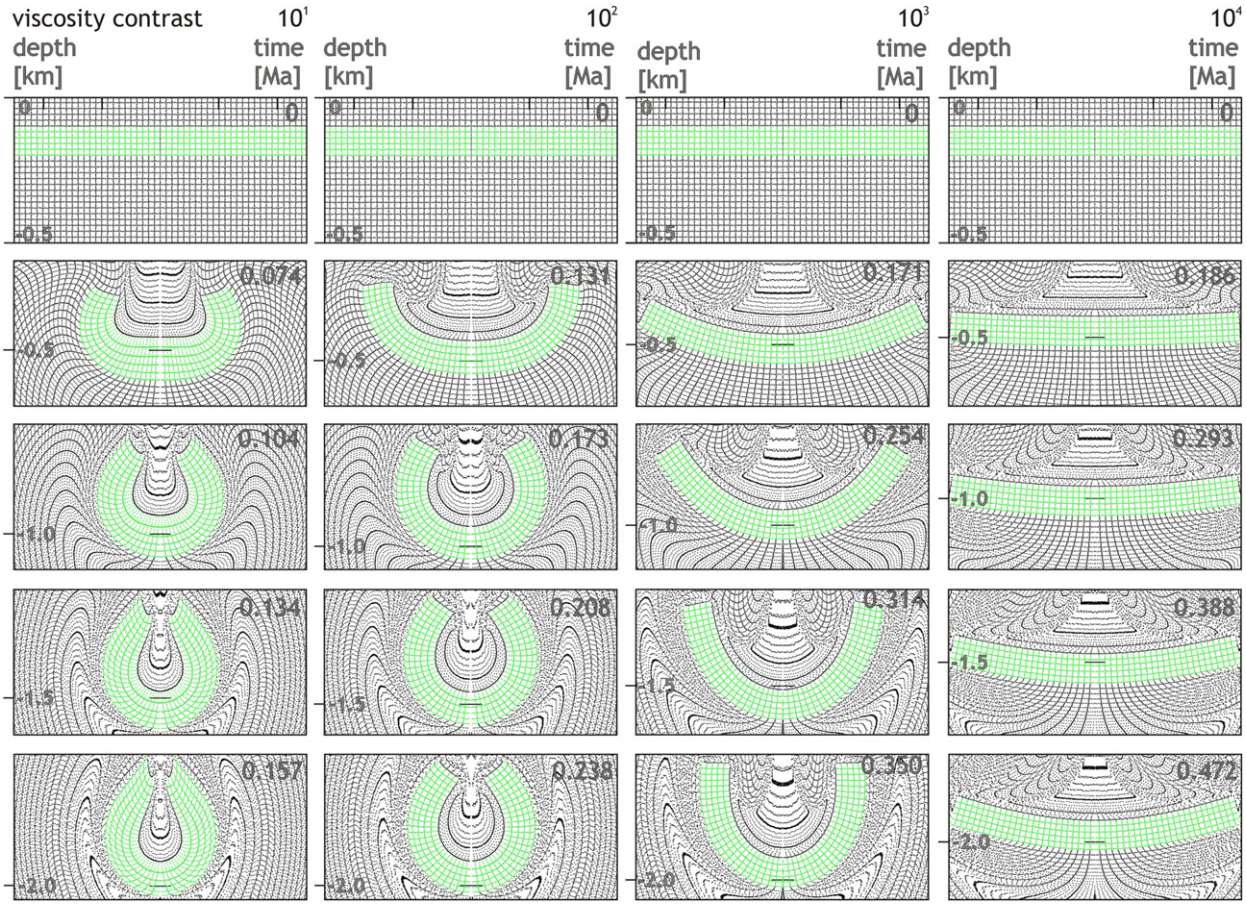

Fig. 5. Sections (1000 m wide and 500 m deep) of mesh plots displaying the strain pattern of a block (in green) with an AR of 1:10 sinking through a matrix of salt (black). The salt has a viscosity of 10^{17} Pa s, while the viscosity of the block varies in each series of models. The mesh plots display every fourth marker of the marker field of the models. (For interpretation of the references to colour in this figure legend, the reader is referred to the web version of this article.)

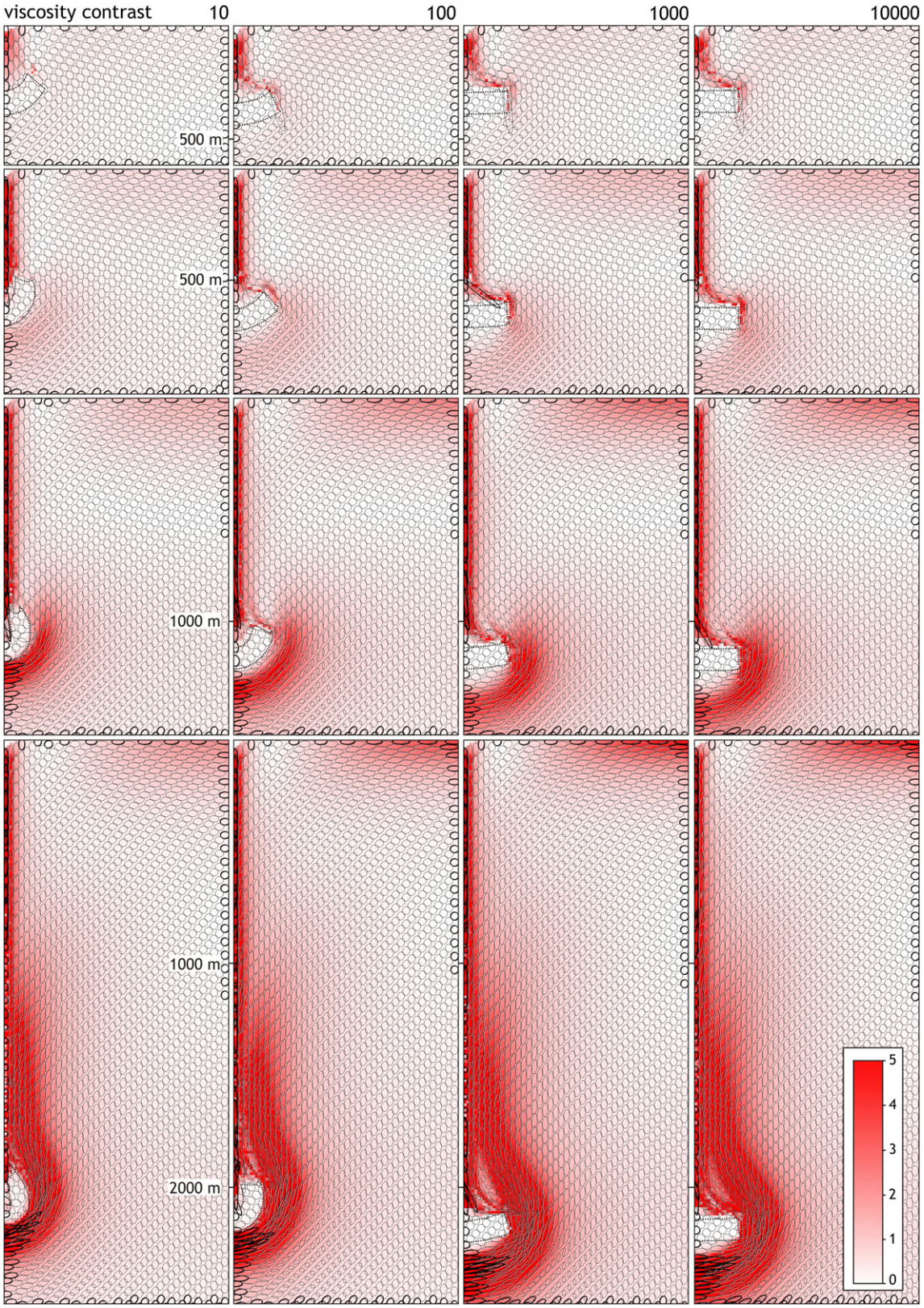

Fig. 6. Strain history in the models with a block AR of 1:4 as a function of the viscosity contrast. Shear strain magnitudes γ (in a grid with a cell size of approximately 12 m) and strain ellipses (only shown for every 10th cell, size reduced to 25%) calculated with the grid nearest-neighbour method in SSPX (Cardozo and Allmendinger, 2009) with a grid spacing of 0.003, 9 nearest neighbours, and a maximum distance of grid points of 0.01, based on the coordinates of 100,000 marker points after (from the top down) 100, 500, 1000, and 2000 m of sinking. Dotted lines trace the block outlines.

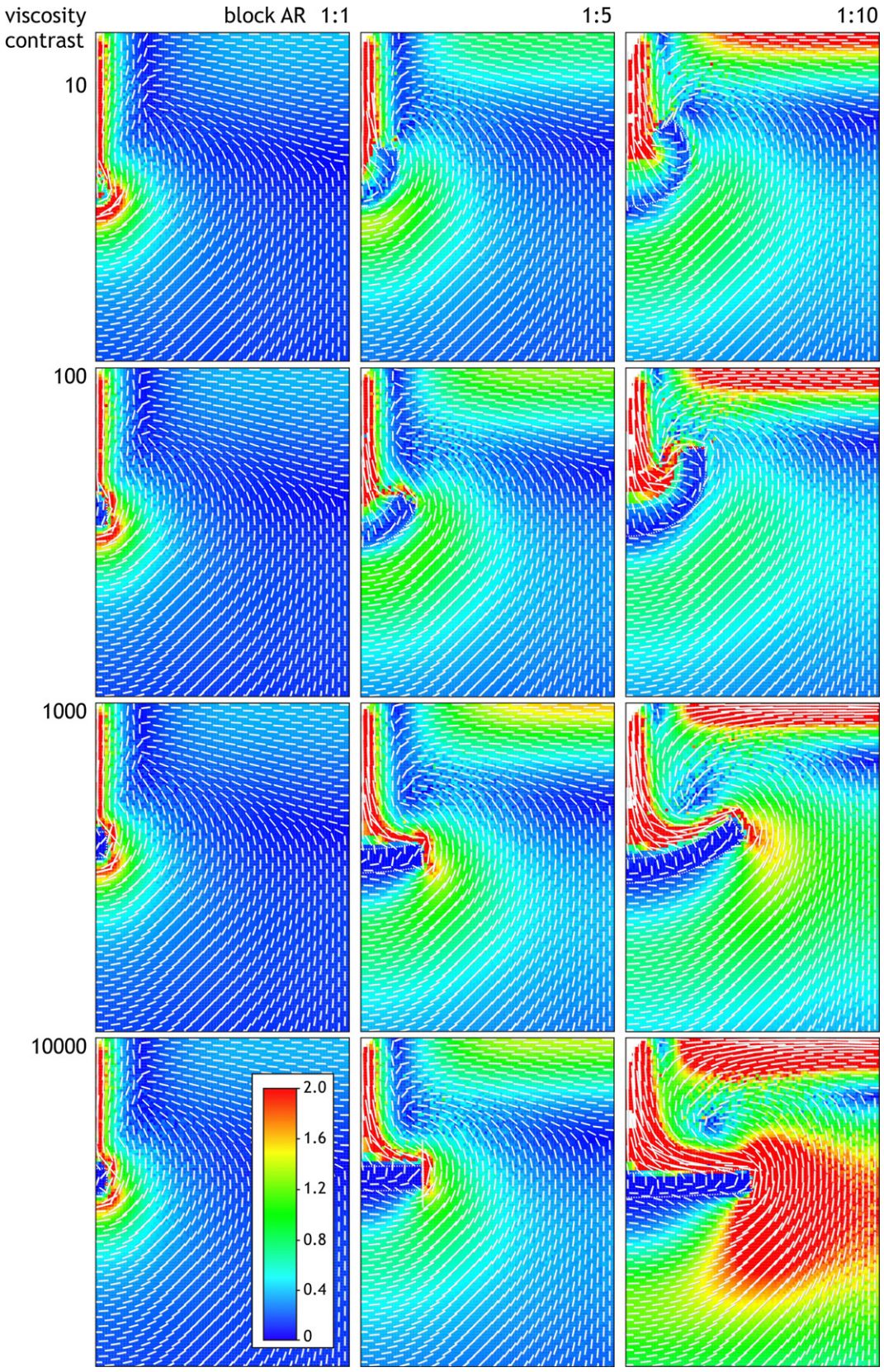

Fig. 7. Magnitudes (in a grid with a cell size of approximately 12 m) and orientation (white ticks, only shown for every 10th cell, scaled to 50% of their length) of extensional strain in models with block ARs of 1:1, 1:5, and 1:10 for viscosity contrasts of 10–10,000. Dotted lines trace the block outlines. Strain magnitudes were calculated with the grid nearest-neighbour method in SSPX (Cardozo and Allmendinger, 2009) with a grid spacing of 0.003, 9 nearest neighbours, and a maximum distance of grid points of 0.01, based on the coordinates of 100,000 marker points after 500 m of sinking of the block.

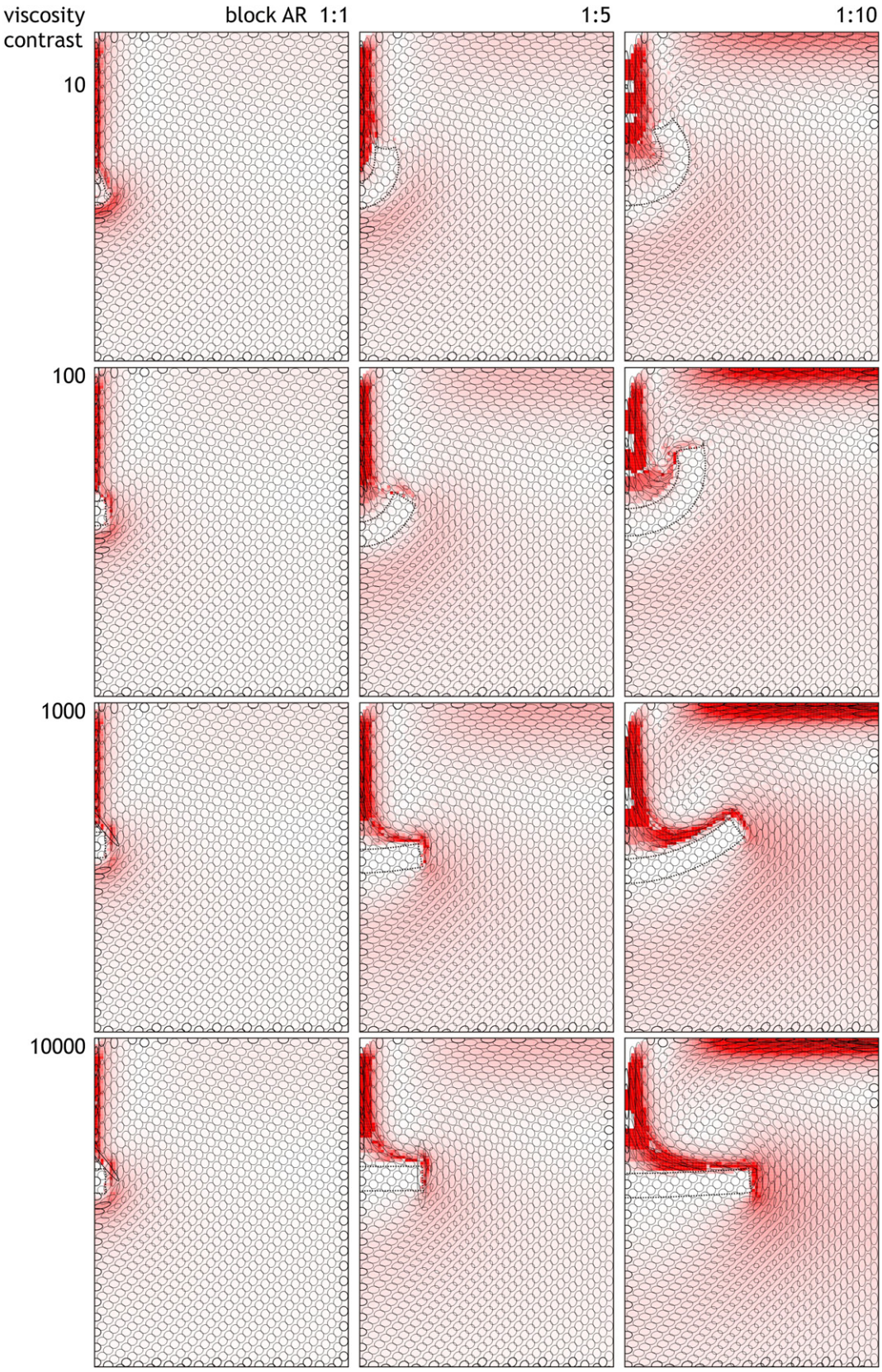

Fig. 8. Maximum shear strain magnitudes γ (in a grid with a cell size of approximately 12 m) and strain ellipses (only shown for every 10th cell, size reduced to 25%) of extensional strain in models with block ARs of 1:1, 1:5, and 1:10 for viscosity contrasts of 10–10,000. Dotted lines trace the block outlines. Strain magnitudes were calculated with the grid nearest-neighbour method in SSPX (Cardozo and Allmendinger, 2009) with a grid spacing of 0.003, 9 nearest neighbours, and a maximum distance of grid points of 0.01, based on the coordinates of 100,000 marker points after 500 m of sinking of the block.

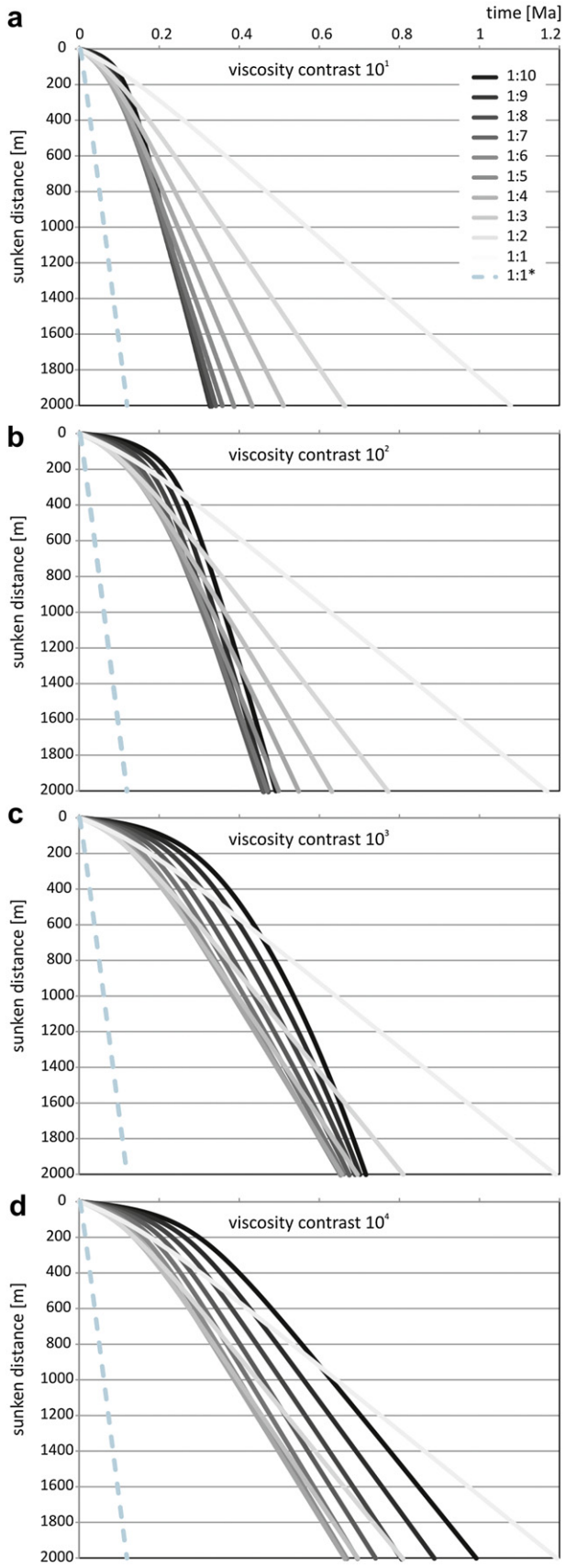

Fig. 9. Vertical position of the centre of the blocks as a function of time. The dashed line illustrates the velocity pattern of a block with an AR of 1:10 but the same mass as the block with an AR of 1:10. Velocity pattern of the model series with a viscosity contrast of a) 10, b) 100, c) 1000, and d) 10,000 between block and matrix material.

1:1 in the model series with $m = 10$ sinks steadily to reach a velocity of 1.86 mm a^{-1} (Fig. 10) after 2000 m sinking. The early phase of acceleration corresponds to the most severe phase of deformation of the block. With increasing block AR, the initial phase of acceleration becomes longer compared to the duration of sinking, which is in accordance with the duration of the most severe block deformation. In the $m = 10$ series, the maximum velocity of the block (after 2000 m of sinking) increases with increasing block AR to 6.11 mm a^{-1} (AR 1:10; Fig. 10). The sinking velocity in this series is therefore a function of the block mass and of the deformation of the block. This is supported by a test model with a block with an AR of 1:1 but the same excess mass ($2200 + 10 \times 700$ kg) as the block with an AR of 1:10 (10 times the excess density of the block with an AR of 1:1). The shape of the velocity curve of this high-density block is the same as that of the smallest block in this series but with a much steeper slope, i.e. the block sinks much faster (Fig. 9). Its maximum velocity after 2000 m of sinking is 18.7 mm a^{-1}, i.e. 10 times faster than the block with an AR of 1:1, but only 3.1 times faster than the block with an AR of 1:10.

In the model series characterised by $m = 100$, the velocity of the block with an AR of 1:1 is characterised by initial acceleration during the first ~0.3 Ma before it sinks in a steady state reaching a final velocity of 1.71 mm a^{-1} (Figs. 9 and 10). This is only slightly slower than the 1:1 block with $m = 10$, as the drag coefficient of a square rod sinking in a container 10–100 times its diameter is only a few percent (2–7%) larger than that of a circular rod of the same cross-sectional area. Towards higher block ARs, the velocity during the initial acceleration phase decreases, while the duration of this phase increases (Fig. 9) probably as a result of the interaction of the block with the upper model boundary. This corresponds to the duration of block deformation to reach the streamlined horseshoe geometry. The influence of the deformation phase therefore increases with increasing block AR so that steady-state sinking is reached later. In comparison with the velocity pattern of a test model with a block with an AR of 1:1 and a mass equal to that of the block with an AR of 1:10, it is obvious that the influence of the increased mass of the larger blocks is secondary compared to the block shape (AR) and the change in shape, respectively. The velocity during decent of the block in the test model resembles that of the block with an AR of 1:1, but with a steeper slope so that it sinks with a velocity 10 times that of the block with an AR of 1:1 and 4.2 times that of the block with an AR of 1:10 and reaches a maximum velocity of 65.48 mm a^{-1} (Fig. 9). The influence of the shape on the velocity pattern applies particularly to the blocks with an AR of >1:7. Consequently, the maximum velocity of all blocks of this model series shows an increase with increasing block AR to 4.36 mm a^{-1} (AR 1:7) to decrease then to 4.07 mm a^{-1} (AR 1:10; Fig. 10).

The velocity pattern of the blocks in the model series with $m = 1000$ shows a distinct influence of block folding. While the block with an AR of 1:1 goes over to steady-state sinking after an acceleration phase of approximately 0.15 Ma, the duration of the acceleration phase is considerably longer for the block with an AR of 1:5 (ca. 0.2 Ma). For blocks with ARs >1:5, the duration of the acceleration phase is even longer so that larger blocks reach steady-state sinking only during the last few hundred metres of their sinking (Fig. 9). This is reflected in the maximum velocities of the blocks that increase from 1.68 mm a^{-1} (AR 1:1) to 3.07 mm a^{-1} (AR 1:5) to decrease to 2.80 mm a^{-1} (AR 1:10) towards higher block ARs (Fig. 10). In comparison, the block in the test model with an AR of 1:10 and the same excess mass as the block with an AR of 1:10 reaches a maximum velocity of 64.41 mm a^{-1}, following a velocity pattern similar to that of the block with an AR of 1:1 in the model series (Fig. 9). It sinks thus 10 times faster than the block with an AR of 1:1 and 6 times faster than the block with an AR of 1:10.

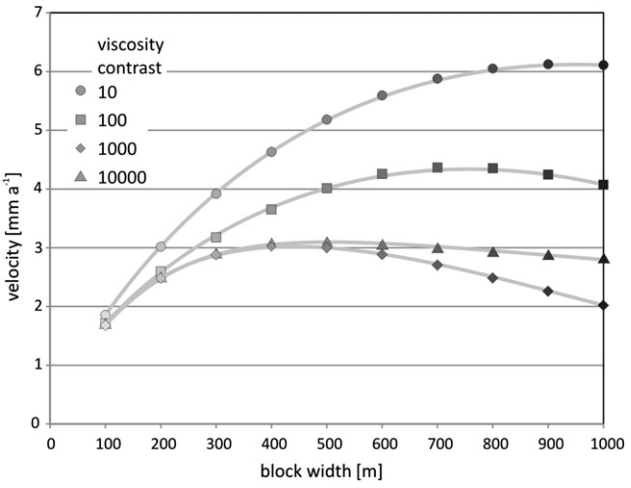

Fig. 10. Maximum velocity of the blocks of all model series as a function of block width after sinking 2000 m.

In the model series with $m = 10{,}000$, the velocity of the blocks indicates that the deformation of the block and the mass increase with increasing block AR are not the only parameters to be considered. While the block with an AR of 1:1 starts its steady-state sinking after a comparatively weakly pronounced acceleration phase of <0.2 Ma to reach a maximum velocity of 1.68 mm a^{-1}, the block with an AR of 1:5 shows a more pronounced acceleration phase of ~0.2 Ma duration (Fig. 9). Its maximum velocity of 3.00 mm a^{-1} is slightly less than the maximum velocity of blocks in this series (3.02 mm a^{-1}; AR 1:4; Fig. 10). Towards higher block ARs, the acceleration phase becomes more pronounced and prolonged, while velocities of the blocks decrease during the acceleration phase and steady-state sinking (Fig. 10). Hence, the maximum velocity of the block with an AR of 1:10 is 2.02 mm a^{-1}. The test model with a block with an AR of 1:1 and the same excess mass as the block with an AR of 1:10 shows that mass increase results in a maximum velocity of 64.20 mm a^{-1} (Fig. 9), which is 10 times faster than the block with an AR of 1:1 and 8.4 times faster than the block with an AR of 1:10. The velocity pattern of the blocks with large ARs can therefore not be ascribed to their higher mass. In addition, since deformation of the 1:10 block is still progressing even after 2000 m of sinking, the change in velocity after the acceleration phase cannot be explained by the block approaching a streamlined geometry. It might thus be attributed to the successful establishment of structures in the salt that accommodate block sinking (i.e. shear zones and folds; cf. Section 4).

4. Strain pattern and magnitudes in the salt around the sinking block

In all the models, the sinking of the block causes strong deformation of the surrounding salt, distributed in a characteristic pattern. This deformation pattern is described with the help of the marker field, a selection of which is plotted as a mesh to illustrate displacement of passive markers. However, note that this neglects any pre-existing internal structure of the salt. Locally, the magnitude of strain in this pattern is more than two orders of magnitude higher in the salt than in the block and depends on the block AR and m (Figs. 7 and 8).

In the models with $m = 10$, initial sinking of the block is immediately accommodated by horizontal salt flow above the block towards the central axis of the model (termed “inward flow” in Fig. 11). Block sinking causes increasing maximum shear strain γ and vertical shortening below the block (Fig. 6) that initiates horizontal outward flow of the underlying salt. At higher block ARs and m, there is a strain shadow between the lower block margin and the shortened zone in the salt that increases in thickness and width to approximately half the initial block thickness and half the width of the deformed block (Figs. 7 and 8). The salt escapes from under the sinking block and flows upwards and around the block in a highly strained zone (Fig. 6), the width of which depends on the block AR (Figs. 7 and 8). As a result of the described salt flow, an antiformal structure develops next to the block in the salt (“marginal antiform” in Fig. 11). Between the block and the marginal antiform, a synform develops in the salt (termed “marginal synform” in Fig. 11) due to viscous downward drag of the salt together with the sinking block. Above the block, viscous

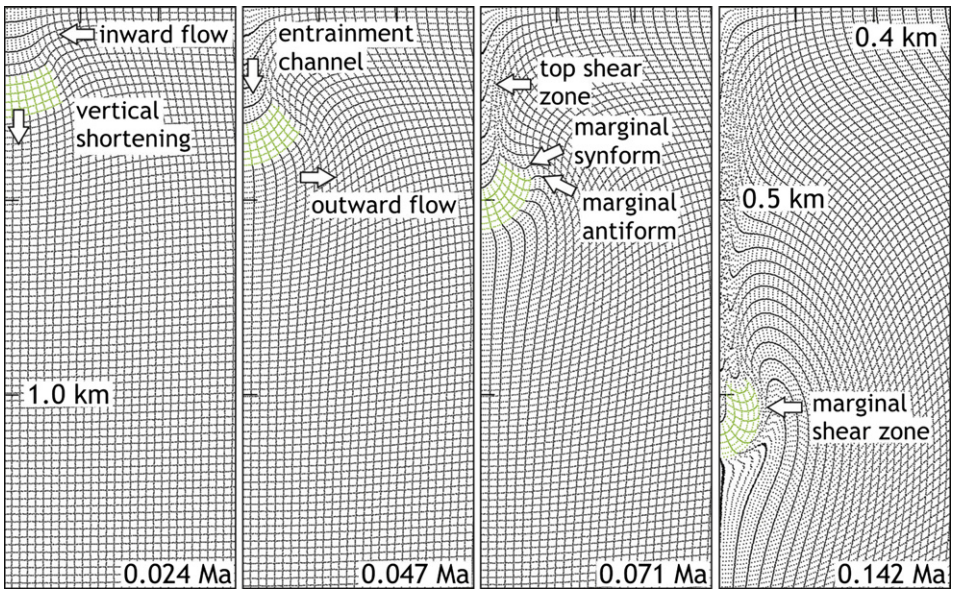

Fig. 11. Formation of typical deformation processes and structures in the salt surrounding a sinking block, 300 m wide. Each image shows a 600 m wide and 1500 m deep section of a mesh plot of a model with a viscosity contrast of 10, i.e., the block is 10 times more viscous than the salt.

downward drag exerts high strains on the salt (Fig. 6) causing the formation of a channel above the block, into which salt is entrained ("entrainment channel", Fig. 11). The entrainment channel forms early during sinking of the block, with a tendency towards an earlier formation (i.e. after less sinking of the block) at higher block ARs. In addition, the width of the entrainment channel increases with increasing block AR (Figs. 7 and 8). In the following, a vertical shear zone forms between the entrainment channel and the adjacent salt ("top shear zone", Fig. 11). After further sinking of the block, a shear zone develops in the salt directly along the block side and disrupts the marginal antiform ("marginal shear zone", Fig. 11). However, the timing of formation of this shear zone is not clearly related to the AR of the block (Fig. 11). The overall array of structures comprising shear zones and folds is characterised by an extremely heterogeneous strain distribution with zones of high adjacent to low strains (Fig. 6).

Deformation processes and structures, their succession of formation, as well as the distribution of strain in the salt surrounding the sinking blocks in the other model series are similar to those described above for $m = 10$ (Figs. 7, 8, and 12). Differences occur in the strain magnitude that not only increases during sinking and with increasing block AR, but also with increasing m up to almost stable strain magnitudes for $m \geq 1000$ (e.g. Fig. 12), a viscosity ratio at which the blocks may be regarded as quasi rigid (cf. Treagus, 2002). Furthermore, the absolute timing of formation, i.e. after what distance of sinking of the block a structure forms, varies with block AR and m. Structures, the time of formation of which is clearly influenced by the block AR, include the entrainment channel and the marginal antiform, as well as in case of some model series, the marginal synform, the top and the marginal shear zone. In order to form an entrainment channel, the block has to sink deeper at higher block ARs independent of m. In contrast, the timing of formation of other structural features does not show a clear relationship with the block AR or m. For example the marginal shear zone in the model series with $m = 10{,}000$ forms earlier at high block ARs, while in the model series with $m = 100$, it forms earlier at low block ARs. Accordingly, the salt is deformed after considerably lower sunken distances of the block at higher m. This is particularly evident in case of the formation of the marginal shear zone and might be an effect of the block's resistance to deformation at higher viscosities so that most of or all the deformation is taken up by the salt.

5. Discussion

The variety of rock types entrained in salt diapirs (e.g. anhydrite, limestone, rhyolite, basalt) implies a wide range of mechanical and rheological properties. The latter have an influence on the deformation behaviour of the inclusions themselves and their surrounding salt. According to e.g. Schmeling et al. (1988) and Cruden (1990), the contrast in viscosity between a buoyancy-driven object and the surrounding material is a main parameter in

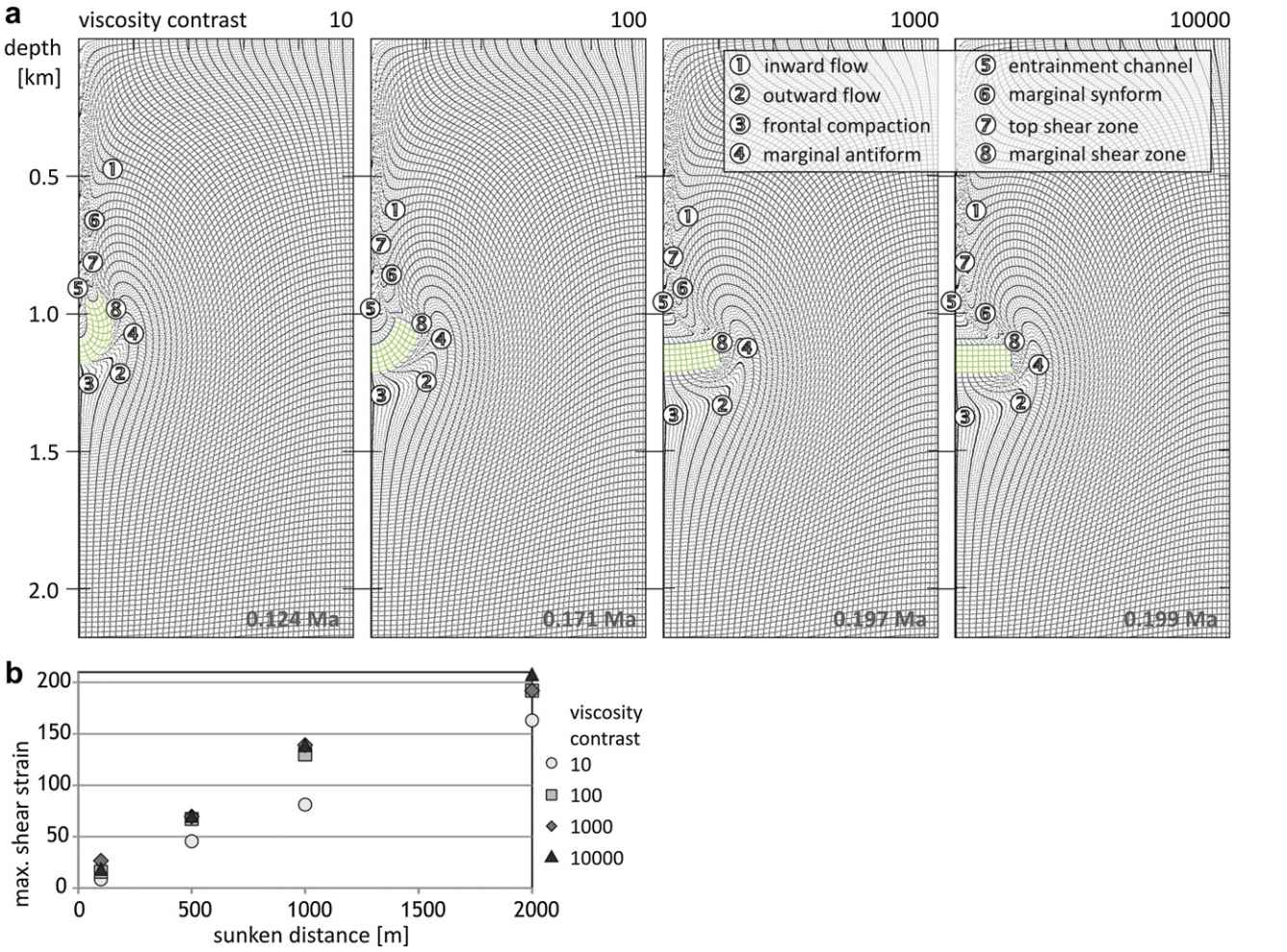

Fig. 12. a) Comparison of deformation processes and structures in the salt surrounding a block with an AR of 1:4 after sinking approximately 1000 m for viscosity contrasts of 10–10,000. b) Maximum shear strain γ in the models in a) after 100, 500, 1000, and 2000 m of sinking. For strain distribution compare Figs. 6–8.

controlling deformation of the system. For this reason, our models covered viscosity contrasts between the inclusion and the salt over four orders of magnitude. In natural systems, there may exist heterogeneity of all involved materials and/or occurrence and interaction of several, differently oriented inclusions, which have to be taken into consideration. However, even though heterogeneity in the mechanical properties is not included, results of the current numerical models can be used to understand the general deformation pattern and distribution in these systems.

From the strain pattern of the sinking blocks in our models, three main elements that control the sinking process and the velocity of blocks sinking through a less viscous host material can be identified: (1) the mass of the block (gravity), (2) block deformation, and (3) matrix deformation, i.e. how the host material accommodates the sinking of the block. These factors are both a function of the block AR and m. The block AR controls parameter (1) and to some extent parameter (2) as well; the mass of the block increases with block AR while the height is kept constant, as well as its size to a horizontally elongate shape that is more easily deformable. Block deformation is achieved by two main mechanisms: folding and marginal shear that are a consequence of viscous drag exerted by the flow of the salt around the block. The viscosity contrast m controls parameters (2) and (3), because a decrease in the viscosity contrast leads to more intense deformation of the block, which accommodates more strain. Conversely, increasing m reduces the strain of the block so that at high m, the blocks do not deform into a streamlined shape. Instead, they sink as more or less horizontal, rectangular slabs resulting in deformation of a larger area within the salt. Accordingly, in the models with the highest viscosity contrast and the highest block AR, strain within the salt is distributed over the largest area.

A comparison of the sinking velocity of all models shows that each block experiences an initial phase of acceleration followed by a phase of steady-state sinking (Fig. 9). At small block ARs, the velocity during the acceleration phase is close to the velocity during steady-state sinking, while at intermediate to large block ARs, the acceleration phase is more pronounced with lower velocities and a longer duration; this is caused by the effect of the top boundary of the model. Within one series of models (constant m), the maximum velocity of the block tends to increase with increasing block AR (Fig. 10), as would be expected for gravity-driven sinking. However, only in the model series with $m = 10$ is the block with the largest excess mass also the one with the highest final velocity. In all other model series, the highest final velocities occur at intermediate block ARs (1:4–1:7). Hence, mass is not the only parameter controlling the sinking velocity of the blocks, instead, the initial tabular geometry seems to have a significant impact on their sinking velocity. This is supported by the velocities of the high-excess density blocks in the test models (Fig. 9). At increasing salt viscosity, the decrease in sinking velocity of high-AR blocks might also partly be affected by the closeness to the side boundaries of the model.

A comparison of the maximum velocities of the blocks in all model series shows that after 2000 m of sinking, all blocks with an AR of 1:1 reach similar velocities (between 1.68 and 1.86 mm a^{-1}) irrespective of m (Fig. 10). In contrast, the maximum velocities of all other blocks in the four series of models differ considerably with changing m. The highest velocities are reached in models with the lowest viscosity contrast (max. velocity of all blocks in all series: 6.11 mm a^{-1} (block AR 1:10, $m = 10$)). Consequently, the maximum velocities decrease with increasing m. However, this does not apply to the model series with $m = 10{,}000$, where the maximum velocities are slightly higher compared to those in the model series with $m = 1000$. The model series with $m = 10{,}000$ is characterised by the lowest intensities of block deformation during sinking. The velocity patterns of the blocks are characterised by a longer acceleration phase preceding steady-state sinking. This can, however, not be related to block deformation as in the other model series. Hence, formation and development of structures in the salt probably also have a significant influence on the velocity pattern of a sinking block, in this case where the block does not deform so much.

To summarise the driving and retarding effects, we identify three characteristic effects regarding the sinking velocity: (1) The sinking velocity increases with the magnitude of the excess density. (2) It decreases with increasing AR (within a confined container of fixed width, such as a salt diapir). (3) It increases with the magnitude of deformation of the block. For a high block viscosity, (3) is negligible, while (1) and (2) act in opposite senses: As long as the container walls are far away, (1) dominates, but when the block edges are closer to the walls, (2) outpaces (1) and the velocity decreases again (Fig. 10). Increasing deformation (3), however, counteracts effect (2) and effectively decreases the drag coefficient, increasing the sinking velocity.

Salt deformation around the block is characterised by increasing strain heterogeneously distributed (Figs. 6–8) across an array of characteristic structures (Fig. 11), the spatial arrangement of which is independent of m and the block AR. These structures include shear zones and folds, as well as a zone characterised by extreme vertical stretching above the sinking block (entrainment channel). The most intensive deformation with the highest strain magnitudes is restricted to the area immediately surrounding the sinking block (Figs. 6–8). The size of the structures forming in the matrix medium depends largely on the size of the sinking block, i.e. its AR, and its deformation behaviour. This implies that increasing the block AR at constant m, results in an increase in the strained area within the salt and the size of the resulting structures. The timing of formation of individual structures does not follow linear relationships with the block AR or m. Instead, the interaction of both parameters is complex and controls when and in what way deformation occurs in the salt.

The results of our two-dimensional models can be applied to natural (i.e. three-dimensional) systems by taking into account that salt structures are often elongate, for example, the Gorleben salt diapir that is 2–4 km wide and about 14 km long, so that the structures that are observed in cross section extend probably for almost that distance in the third dimension. Hence, plain-strain models may be, at least qualitatively, applied to understand deformation of anhydrite blocks and the surrounding salt to identify the effect of gravitational sinking as compared to ascent- and entrainment-related deformation. Furthermore, the orientation of the strain ellipses in our models is compatible with those of the strain ellipsoids around a sphere rising (or falling) in a viscous medium, calculated by Schmeling et al. (1988). In this latter case, our two-dimensional models simulate and show the profile of an axisymmetric body (e.g. Stokes sphere) sinking within a viscous medium.

Our model results yield implications for other gravity-driven systems that can be approximated by a suspension flow, such as crystals surrounded by melt in magmatic bodies. According to Kerr and Lister (1991) and Arbaret et al. (2000), the latter can be approximated as a dynamic suspension of rigid particles, the crystals, in an initially Newtonian matrix, the melt. The mechanical interaction of the crystals with the melt generally follows Stokes equation (Stokes, 1851; Martin and Nokes, 1988). However, as demonstrated by Kerr and Lister (1991) and e.g. Arbaret et al. (2000), it also depends on the shape of the crystals and the fraction of crystals in the system. In these cases, deformation patterns similar to those in our models with high m should be expected. However, since primary magmatic fabrics are seldom preserved at

this scale, the strain pattern produced by a settling crystal is usually not preserved. The same applies to deformation caused by the gravity-driven sinking of wall-rock xenoliths in granitic plutons, the preservation of which depends on the timing relative to solidification of the magma (Fowler and Paterson, 1997; Clarke et al., 1998).

As demonstrated numerically and experimentally by Schmeling et al. (1988) and Cruden (1990), the diapiric rise of mantle plumes, magmatic diapirs, and gneiss domes through viscous surrounding rock can be modelled as the sinking of a higher-density inclusion through a viscous medium. Hence, the modelling results of the processes, mechanisms, and forces related to the sinking of higher-density anhydrite blocks through salt yield implications for the gravity-driven rise of the above mentioned structures. In comparison with natural diapirs that are, in contrast to the blocks in our models, characterised by a lower viscosity than the adjacent material, our model results suggest a remarkable difference between weak ($\mu_{inclusion} < \mu_{matrix}$) and strong ($\mu_{inclusion} > \mu_{matrix}$) sinking inclusions: While for a weak inclusion, the finite strain roughly partitions equally inside the inclusion and outside in the stiffer matrix (Figs. 3 and 7 in Schmeling et al., 1988), the opposite is true for a stiff inclusion moving through a weak host material. For high m, most of the finite strain takes place in the weak material and almost no straining occurs in the strong blocks.

Since the sinking of the blocks in our models produces characteristic structures independent of the shape (AR) of the block, it can be assumed that these structures will also be produced by the rise of a magmatic diapir through the mantle or lower crust. In analogy with the marginal shear zone and antiform observed in our models, magmatic diapirs are usually surrounded by a highly strained aureole including ductile shear zones surrounded by a rim syncline. Furthermore, the tail of natural diapirs corresponds to the entrainment channel in our models. As demonstrated by Cruden et al. (1995), entrainment of mafic into felsic magma can occur in case of magmatic diapirs. This is in accordance with the two-dimensional axisymmetrical models by Schmeling et al. (1988) where the highest strains occurred in a narrow tube behind the rising or sinking sphere and in a narrow shell around the sphere. The strain pattern within the sphere modelled by Schmeling et al. (1988) is characterised by oblate strain ellipsoids with the short axis pointing radially away from the rising body. According to Cruden (1990), the internal strain magnitude of a rising (or sinking) sphere is a function of the viscosity contrast between the sphere and the host material, which is supported by our modelling results.

6. Conclusions

The gravity-driven sinking of a dense, rectangular block results in severe deformation of the block itself and the host material it sinks within. Deformation of the block is characterised by folding and shearing as it approaches a streamlined, tear-drop shape that can even incorporate a portion of the initially overlying salt. The intensity of block deformation is a function of the viscosity contrast between the block and the surrounding salt and the block AR. In general, block strain is facilitated in models with a block with high AR and a low m.

The sinking velocity of a block is a function of the block mass, but even more of its deformation behaviour that is influenced by both the block AR and the viscosity contrast. Block sinking is characterised by an initial phase of acceleration with low velocities as long as the block is close to the upper boundary of the salt structure followed by a phase of steady-state sinking. With increasing block AR and viscosity contrast, the velocity during the acceleration phase decreases while its duration increases. This pattern is thus, in its timing and development, dependent on the deformation behaviour of the block but probably also on the deformation of the salt. After 2000 m of sinking, the blocks in our models reach velocities in the range of 2–6 mm a^{-1}.

Host material deformation around the sinking block comprises an array of structures that consists of folds, shear zones, and a narrow zone in the salt above the sinking block, in which extremely high amounts of vertical elongation occur, here termed entrainment channel. This structural array forms independent of the block AR and the viscosity contrast. The size of individual structures is partly dependent on the block AR, while the intensity of deformation is a function of salt viscosity. The latter relation is characterised by decreasing strain magnitudes with increasing salt viscosity, analogous to the strain in the block. The succession of formation of the structures in the matrix salt is more or less the same, independent of the block AR and viscosity contrast. In contrast, the timing of formation, i.e. after what distance of sinking of the block individual structures form, is a function of the complex interaction of both parameters. In general, most deformation structures form early during the first few hundred metres of sinking of the block, but they intensify with time.

Acknowledgements

The authors are grateful to Zurab Chemia and Jochen Kamm for help with data evaluation, the participants of the salt workshop at the TSK13 conference in Frankfurt in 2009 for discussion, and Stuart Hardy for suggesting to use the free software SSPX. The manuscript benefited from detailed reviews by Susan Treagus and Alexander Cruden. Funding was provided by the Swedish Research Council (VR).

References

Arbaret, L., Fernandez, A., Jezek, J., Ildefonse, B., Launeau, P., Diot, H., 2000. Analogue and numerical modelling of shape fabrics: application to strain and flow determination in magmas. Transactions of the Royal Society of Edinburgh: Earth Sciences 90, 97–109.

Bornemann, O., 1991. Zur Geologie des Salzstocks Gorleben nach Bohrergebnissen, vol. 4. Bundesamt für Strahlenschutz Schriften, Saltgitter, Hannover, Germany. 67.

Burchardt, S., Koyi, H., Schmeling, H., 2011. Strain pattern within and around denser blocks sinking within Newtonian salt structures. Journal of Structural Geology 33, 145–153. doi:10.1016/j.jsg.2010.11.007.

Cardozo, N., Allmendinger, R.W., 2009. SSPX: a program to compute strain from displacement/velocity data. Computers & Geosciences 35, 1343–1357.

Chemia, Z., Schmeling, H., Koyi, H., 2009. The effect of the salt viscosity on future evolution of the Gorleben salt diapir, Germany. Tectonophysics 473, 446–456.

Clarke, D.B., Henry, A.S., White, M.A., 1998. Exploding xenoliths and the absence of 'elephants' graveyards' in granite batholiths. Journal of Structural Geology 20, 1325–1343.

Cruden, A.R., 1990. Flow and fabric development during the diapiric rise of magma. The Journal of Geology 98, 681–698.

Cruden, A.R., Koyi, H., Schmeling, H., 1995. Diapiric basal entrainment of mafic into felsic magma. Earth and Planetary Science Letters 131, 321–340.

Fowler, T.K., Paterson, S.R., 1997. Timing and nature of magmatic fabrics from structural relations around stoped blocks. Journal of Structural Geology 19, 209–224.

Gansser, A., 1992. The enigma of the Persian dome inclusions. Eclogae Geologica Helvetica 85, 825–846.

Gansser, A., 1960. Über Schlammvulkane und Salzdome. Vierteljahresschrift Naturforscher Gesellschaft Zürich 105, 1–46.

Jackson, M.P.A., Cornelius, R.R., Craig, C.H., Gansser, A., Stocklin, J., Talbot, C.J., 1990. Salt diapirs of the Great Kavir, Central Iran. Geological Society of America Memoir 177 139pp.

Kent, P.E., 1979. The emergent Hormuz salt plugs of southern Iran. Journal of Petrological Geology 2, 117–144.

Kerr, R.C., Lister, J.R., 1991. The effects of shape on crystal settling and on the rheology of magmas. The Journal of Geology 99, 457–467.

Koyi, H., 2001. Modeling the influence of sinking anhydrite blocks on salt diapirs targeted for hazardous waste disposal. Geology 29, 387–390.

Martin, D., Nokes, R., 1988. Crystal settling in a vigourously convecting magma chamber. Nature 332, 534–536.

Mukherjee, S., Talbot, C.J., Koyi, H.A., 2010. Viscosity estimates of salt in the Hormuz and Namakdan salt diapirs, Persian Gulf. Geological Magazine 147, 497–507.

Müller, P., Siemes, H., 1974. Festigkeit, Verformabarkeit und Gefügeregelung von Anhydrit – Experimentelle Stauchverformung unter Manteldrucken bis 5 kbar bei Temperaturen bis 300°C. Tectonophysics 23, 105–127.
Müller, W.H., Schmid, S.M., Briegel, U., 1981. Deformation experiments on anhydrite rocks of different grain sizes: rheology and microfabric. Tectonophysics 78, 527–543.
Peters, J.M., Filbrandt, J.B., Grotzinger, J.P., Newall, M.J., Shuster, M.W., Al-Siyabi, H.A., 2003. Surface-piercing salt domes of interior North Oman, and their significance for the Ara carbonate "stringer" hydrocarbon play. GeoArabia 8, 231–270.
Ramsay, J.G., Huber, M.I., 1987. The techniques of modern structural geology: folds and fractures. Academic Press, 391 pp.
Reuning, L., Schoenherr, J., Heimann, A., Urai, J.L., Littke, R., Kukla, P., 2009. Constraints on the diagenesis, stratigraphy and internal dynamics of the surface-piercing salt domes in the Ghaba salt basin (Oman): a comparison to the Ara formation in the South Oman salt basin. GeoArabia 14, 83–120.
Schmeling, H., Cruden, A.R., Marquart, G., 1988. Progressive deformation in and around a fluid sphere moving through a viscous medium: implications for diapiric ascent. Tectonophysics 149, 17–34.
Schoenherr, J., Schleder, Z., Urai, J.L., Littke, R., Kukla, P.A., 2010. Deformation mechanisms of deeply buried and surface-piercing Late Pre-Cambrian to Early Cambrian Ara Salt from interior Oman. International Journal of Earth Sciences 99, 1007–1025.
Stokes, G.G., 1851. On the effect of the internal friction of fluids on the motions of pendulums. Transactions of the Cambrian Philosophical Society 9, 1.
Treagus, S.H., 2002. Modelling the bulk viscosity of two-phase mixtures in terms of clast shape. Journal of Structural Geology 24, 57–76.
Urai, J.L., Spiers, C.J., Zwart, H.J., Lister, G.S., 1986. Weakening of rock salt by water during long-term creep. Nature 324, 554–557.
Urai, J.L., Schléder, Z., Spiers, C.J., Kukla, P.A., 2008. Flow and transport properties of salt rocks. In: Littke, R., Bayer, U., Gajewski, D., Nelskamp, S. (Eds.), Dynamics of Complex Intracontinental Basins: The Central European Basin System. Springer-Verlag, Berlin, Heidelberg, pp. 277–290.
Weinberg, R.F., 1993. The upward transport of inclusions in Newtonian and power-law salt diapirs. Tectonophysics 228, 141–150.
Weinberg, R.F., Schmeling, H., 1992. Polydiapirs: multiwavelength gravity structures. Journal of Structural Geology 14, 425–436.
Zulauf, G., Zulauf, J., Bornemann, O., Kihm, N., Peinl, M., Zanella, A., 2009. Experimental deformation of a single-layer anhydrite in halite matrix under bulk constriction. Part 1: Geometric and kinematic aspects. Journal of Structural Geology 31, 460–474.